SANDIA REPORT
SAND2022-XXXX
Printed September 2022

Sandia National Laboratories

Computational Analysis of Coupled Geoscience Processes in Fractured and Deformable Media

Hongkyu Yoon, Alec Kucala, Kyung Won Chang, Mario J Martinez, James E Bean, Teeratorn Kadeethum, Maria Warren, Jennifer Wilson, Scott T Broome, Lauren K Stewart, Diana Estrada, Nicholas Bouklas, and Jan N Fuhg

Prepared by
Sandia National Laboratories
Albuquerque, New Mexico
87185 and Livermore,
California 94550

Issued by Sandia National Laboratories, operated for the United States Department of Energy by National Technology & Engineering Solutions of Sandia, LLC.

Available to DOE and DOE contractors from
U.S. Department of Energy
Office of Scientific and Technical Information
P.O. Box 62
Oak Ridge, TN 37831

Telephone: (865) 576-8401
Facsimile: (865) 576-5728
E-Mail: reports@osti.gov
Online ordering: http://www.osti.gov/scitech

Available to the public from
U.S. Department of Commerce
National Technical Information Service
5301 Shawnee Rd
Alexandria, VA 22312

Telephone: (800) 553-6847
Facsimile: (703) 605-6900
E-Mail: orders@ntis.gov
Online order: https://classic.ntis.gov/help/order-methods/

ABSTRACT

Prediction of flow, transport, and deformation in fractured and porous media is critical to improving our scientific understanding of coupled thermal-hydrological-mechanical processes related to subsurface energy storage and recovery, nonproliferation, and nuclear waste storage. Especially, earth rock response to changes in pressure and stress has remained a critically challenging task. In this work, we advance computational capabilities for coupled processes in fractured and porous media using Sandia Sierra Multiphysics software through verification and validation problems such as poro-elasticity, elasto-plasticity and thermo-poroelasticity. We apply Sierra software for geologic carbon storage, fluid injection/extraction, and enhanced geothermal systems. We also significantly improve machine learning approaches through latent space and self-supervised learning. Additionally, we develop new experimental technique for evaluating dynamics of compacted soils at an intermediate scale. Overall, this project will enable us to systematically measure and control the earth system response to changes in stress and pressure due to subsurface energy activities.

ACKNOWLEDGEMENTS

This work was supported by the Sandia National Laboratories Laboratory Directed Research and Development program, Project No. 218328. We thank Dr. Moo Lee (retired) for his advice in project idea development and support and Dr. Austin A. Holland for project management.

CONTENTS

LIST OF FIGURES

This page left blank

ACRONYMS AND TERMS

Acronym/Term	Definition
THMC	thermal-hydrological-mechanical-chemical
ES	Earth science
SM	Solid mechanics
1D	one-dimensional
FC	fully coupled
FS	fixed stress
microCT	micro-computed tomography
mD	milliDarcy
CFL	Courant–Friedrichs–Lewy
ROM	reduced order model
PDEs	partial differential equations
DL	deep learning
CcGAN	continuous conditional generative adversarial networks
POD	proper orthogonal decomposition
CNN	convolutional neural network
DC-AE	deep-convolutional autoencoders
CPINN	convolutional physics-informed neural network
DCRM	deep convolutional ritz method
BT-ROM	Barlow twins reduced order modeling
UQ	uncertainty quantification
DIC	digital image correlation

This page left blank

1. INTRODUCTION

Prediction of flow, transport, and deformation in fractured and porous media is critical to improving our scientific understanding of coupled thermal-hydrological-mechanical-chemical (THMC) processes across various subsurface energy storage and recovery activities, nonproliferation activities, and nuclear waste storage. The path-dominant and discontinuous features of fractured media pose significant challenges to understanding and controlling of many national security and subsurface energy activities. Despite the significant amount of works [e.g., Faybishenko et al., 2015; Berre et al., 2018], our current understanding of flow and transport in fractured and deformable media is inadequate to effectively characterize, predict, or control multiphysics processes with confidence or in real-time. Thus, research needs exist to explicitly address the physical mechanisms underlying complex behavior in fractured and deformable media.

Over the past decades various numerical methods (e.g., finite element, finite difference methods, and their variants) have been developed and used to simulate multiphysics processes in the subsurface (flow, transport, mechanical deformation, etc.). Earth science (ES) computational codes for flow, transport, geomechanics, and chemical reaction have been mostly driven by various research programs including fossil energy, waste disposal, renewable energy, and basic energy science programs. Moreover, new emerging computational advances in next generation scientific computing (e.g., exascale high performance computing) and machine learning methods change the landscape for simulating complex, dynamic, and non-stationary processes (meshing, solver, scalability, utilities, etc.). In addition, the earth rock response to changes in pressure and stress have remained a critically challenging task.

A primary goal of this project is to advance computational capabilities for coupled thermo-hydro-mechanical processes in fractured and porous media, integration of high-fidelity predictive simulation with experimental data, and machine learning approach. To achieve the goal, we aim to develop problem sets for verification of Sandia Sierra Multiphysics software, applications of Sierra software for realistic problems involving coupled poromechanics, and synthetic cases of coupled processes for machine learning development. For verification, we use benchmark problems that account for multiple coupled processes such as poro-elasticity, elasto-plasticity, and thermo-poroelasticity. In addition, well-controlled experimental results in fractured and porous media are used to characterize fracture and porous media response under mechanical confinement. For field applications of high fidelity model, we aim to tackle timely topics related to subsurface energy activities such as geologic carbon storage for carbon management and fluid injection and extraction systems for enhanced geothermal systems and wastewater injection. For machine learning development, we utilize numerical simulation of high fidelity models to generate synthetic data for coupled processes such as poroelasticity and thermo-hydro processes. In particular, we aim to improve learning process using advanced concept such as self-supervised learning. Additionally, we develop new experimental technique for evaluating dynamics of compacted soils at an intermediate scale in higher-rate loading regimes. Experimental results can be used to link mechanical properties of soil samples under quasi-static and dynamic conditions.

Overall, this project will enable us to systematically measure the effects of hydrogeological and mechanical characteristics of fractured and deformable media on the earth system response (e.g., flow and stress). This project will deliver the following major outcomes: (1) a merged framework for tightly coupled high-fidelity simulations, (2) verification and validation of Sierra Multiphysics software, (3) various machine learning-based surrogate models for coupled ES processes, and (4) a new experimental capability of measuring earth material response under impact testing.

This page left blank

2. COMPARISON OF NUMERICAL COUPLING APPROACHES FOR COUPLED BENCHMARK PROBLEMS

2.1. Poroelasticity

Coupled processes involving solid response in the subsurface system can be started from poroelasticity where poroelasticity theory describes the simultaneous solid-skeleton deformation and pore fluid flow of a porous medium (Verruijt, 2015). The governing equations used to describe these coupled processes include equilibrium equations of the porous medium and equations of mass conservation for its constituents (solids and pore fluid). Terzhagi (1923) pioneered the study of one-dimensional consolidation, initially considering a porous medium with incompressible constituents and Biot (1941) extended this work to compressible constituents and three-dimensional problems and later to dynamic and nonlinear elastic behavior. The detailed history of poroelasticity and key contributions and assumptions are available in the literature (e.g., Wang, 2000; Verruijt, 2015; Merxhani, 2016). Here, we briefly summary the key equations used in the study.

The total stress (σ_{ij}) on a porous medium can be decomposed into two components: portions of stress distributed to solid skeleton and the pore fluid, respectively (Terzhagi, 1943). The effective stress (σ'_{ij}) concept for mechanical deformation with tensile stress as positive is defined by

$$\sigma_{ij} = \sigma'_{ij} - \alpha p \delta_{ij} \tag{2-1}$$

where $\alpha p \delta_{ij}$ represents the portion of stress that is distributed to the pore fluid, α is the Biot coefficient, p is the pore pressure and positive with compression, and δ_{ij} the Kronecker delta. The momentum equilibrium relation in the drained conditions is

$$\left(K + \frac{1}{3}G\right)\frac{\partial \epsilon}{\partial x_i} + G\nabla^2 u_i = \alpha \frac{\partial \mathrm{p}}{\partial x_i} - b_i \tag{2-2}$$

where K is the bulk modulus, G is the shear modulus, ϵ is the volumetric strain, x_i the coordinate reference frame, u_i is the displacement, b_i are the body forces. The mass conservation equation with Darcy's law for fluid flow is

$$\alpha \frac{\partial \epsilon}{\partial t} + S_e \frac{\partial p}{\partial t} = -\nabla \cdot \mathbf{q} \tag{2-3}$$

where $\epsilon\ (= \epsilon_{xx} = \epsilon_{xx} + \epsilon_{yy} + \epsilon_{zz})$ is the volumetric strain, representing the change in volume per unit volume, S_e is the storativity of pore space, and the seepage velocity ($\mathbf{q}$) is defined as

$$\mathbf{q} = \frac{-k}{\mu}\nabla\left(p - \rho_f \boldsymbol{z} g\right) \tag{2-4}$$

where k is the intrinsic permeability, μ is the dynamic viscosity of the fluid, ρ_f is the fluid density, z is the elevation in depth, and g is the gravity acceleration.

As seen in Equations (2-2, 2-3), these set of equations are coupled through the volumetric strain (hence, the displacement) and pore pressure. Due to its coupling, there are many numerical methods to be studied. In this work we evaluated a few of them in the next section to verify the accuracy and convergency of the coupling scheme.

2.2. Implementation of fixed stress scheme in Sierra Multiphysics software

Using the nodal based displacement (u_i)-pore pressure (p) formulation, there are four solution variables per node including three displacement components and one pore pressure variable that characterize the poroelastic behavior. With the addition of energy transfer, i.e. for the thermo-poroelastic problems an additional nodal temperature is included. This set of equations can be solved simultaneously with a computational method that is often called a fully coupled monolithic solution. The fully coupled monolithic solution procedure requires significant computational resources and a unified thermal-porous flow-mechanics solver with specialized preconditioners for iterative solvers. Alternatively, an identical solution can also be obtained through iteratively coupled methods. In this method, two separate solvers, one for solid mechanics and another for thermal and porous flow can be used and the computational demand is lower because we are solving smaller uncoupled equation sets. The overall speed up on a multiphysics problem depends on the number of coupling iterations, for each time step, being sufficiently small. Among the operator split iterative methods, the fixed-stress scheme is known to be unconditionally stable and computationally efficient (Kim et al., 2011). In our implementation of the fixed stress scheme, the thermal/porous flow problem is solved first while setting the time derivative of total mean stress to zero. Then, the mechanics problem is solved. This process is iterated for each time step until convergence to an acceptable tolerance is obtained. For sufficiently tight convergence tolerance, the fully coupled monolithic solution and the iteratively coupled fixed stress solutions should coincide.

In this work, we use multiple modules in the Sandia Sierra multiphysics software including a thermal/fluid mechanics module (Sierra/Aria, 2021) for treating the thermal/porous flow problem and a solid mechanics module (Sierra/SM, 2021) for treating the deformation problem. It is also possible to solve fully coupled thermo-poroelastic problems using Sierra/Aria in either monolithic or fixed-stress form. Before this project, a loose coupling scheme was the default method to couple multiple modules within the Sierra software, hence, we implemented the fixed stress scheme into both Sierra/Aria and Sierra/SM using a coupling module, Sierra/Arpeggio (2021) for simulating tightly coupled thermo-poroelastic physical systems.

Briefly, this fixed stress scheme solves the system of Equations (2-2 and 2-3). First, at time *t*, the rate of mean total stress is fixed from the solution at the previous iteration when solving the thermal-porous flow equations. In Aria, this is executed using 2 equations (Coussy, 2010): one equation for the porosity ϕ and another for the mean total stress σ:

$$\phi - \phi_0 = \alpha\epsilon + \frac{(\alpha-\phi_0)(1-\alpha)}{K_d}(p - p_0) - 3\alpha_\varphi(T - T_0) \tag{2-5}$$

$$\sigma = K_d\epsilon - \alpha p - 3\alpha_s K_d(T - T_0) \tag{2-6}$$

where ϕ_0 is the initial or reference porosity, K_d is the drained bulk modulus, α is Biot's coefficient, and $3\alpha_\varphi$ and $3\alpha_s$ are the volumetric thermal expansion or dilation coefficients of the pore space and porous solid, respectively. These two thermal coefficients are related according to $\alpha_\varphi = \alpha_s(1 - \phi_0)$. Biot's coefficient α can be expressed in terms of the bulk modulus of the matrix solid K_s and the drained bulk modulus $\alpha = 1 - \frac{K_d}{K_s}$. To complete the parameter definitions, p_0 and T_0 are the reference pore pressure and temperature at which $\epsilon = 0$ and $\phi = \phi_0$.

In the fixed stress scheme, when evaluating the porosity in the thermal/porous flow equations we hold the mean total stress constant between iterations *k* and *k+1*, $\sigma^{k+1} = \sigma^k$. The following expression expresses that constraint:

$$K_d\epsilon^{k+1} - \alpha p^{k+1} - 3\alpha_s K_d(T^{k+1} - T_0) = K_d\epsilon^k - \alpha p^k - 3\alpha_s K_d(T^k - T_0) \quad (2\text{-}7)$$

Solving for ϵ^{k+1}gives

$$\epsilon^{k+1} = \epsilon^k + \frac{\alpha}{K_d}(p^{k+1} - p^k) + 3\alpha_s(T^{k+1} - T^k) \quad (2\text{-}8)$$

Substituting Eq. (2-8) into the first of Eq. (2.7) becomes

$$\phi^{k+1} - \emptyset_0 = \alpha\epsilon^k + \frac{(\alpha-\phi_0)(1-\alpha)}{K_d}(p^{k+1} - p_0) - 3\alpha_\varphi(T^{k+1} - T_0) + \frac{\alpha^2}{K_d}(p^{k+1} - p^k) + 3\alpha\alpha_s(T^{k+1} - T^k) \quad (2\text{-}9)$$

When the sequential method converges, $p^{k+1} - p^k \Rightarrow 0, T^{k+1} - T^k \Rightarrow 0, \quad \epsilon^{k+1} \Rightarrow \epsilon$ and $\phi^{k+1} = \phi$ at time t. In this work, the fixed stress scheme has been implemented into the master version of Sandia Sierra Mechanics software. Examples of the fixed stress scheme for poroelasticitiy and thermo-poroelasticity are reported in the Sections 2.3 and 2.5, respectively. We note that for thermo elastic-plastic problems the parameter K_d and α_s are not constant and can be adjusted based on the local element based elastic-plastic moduli and elastic plastic-thermal moduli, respectively, at the previous time step (Garipov et al., 2018). This option has not been implemented in Sandia Sierra Mechanics software but may be included in the future if elastic-plastic constitutive models are needed.

2.3. Evaluation of accuracy and convergence of numerical coupling approaches for poroelasticity benchmark problems

This work (Warren et al., 2022) is published in the Geomechanics for Energy and the Environment where we evaluated the accuracy and convergence of two fixed stress schemes in Sierra/Aria only and between Sierra/Aria and Sieraa/SM as described Section 2.2. These two fixed stress schemes and the fully coupled method are verified with three poroelasticity benchmark problems including one-dimensional (1D) Terzaghi, 2D Mandel, and 3D Cryer sphere. Detailed equations and references are listed in Warren et al. (2022). In this work the accuracy and convergence of three different coupling schemes with a range of permeability, elastic modulus, and Biot coefficient is evaluated for the pore pressure and displacement. First, we were able to demonstrate that the fixed stress schemes can perform with accuracy similar to the fully coupled scheme, but more computationally efficiently. However, the fixed stress scheme requires the refined numerical tolerance to achieve a target accuracy with low permeable cases. On the other hand, the fixed stress scheme is numerically much more stable than the fully coupled scheme in the low permeable cases where the fully coupled scheme uses finite elements with equal-order interpolation for displacement and pore pressure. After three base benchmark problems, one special case with a two-layer Terzaghi problem was investigated. As shown in Figure 2-1, the fixed stress schemes perform relatively accurately (Figure 2-1a&b) and very accurately (Figure 2-1c-d). For cases in Figure 2-1a&b, the permeability of saline aquifer (A) is lower than that of sandstone (S), requiring slow dissipation of pressure to the top boundary. This causes the numerical accuracy to decrease, requiring the refined tolerance in particular with the fixed stress scheme. The more detailed analysis is provided in Warren et al. (2022). Overall, this work clearly demonstrates that the fixed stress scheme is robust and numerically accurate and stable. Hence, this scheme will be much useful for highly nonlinear problems.

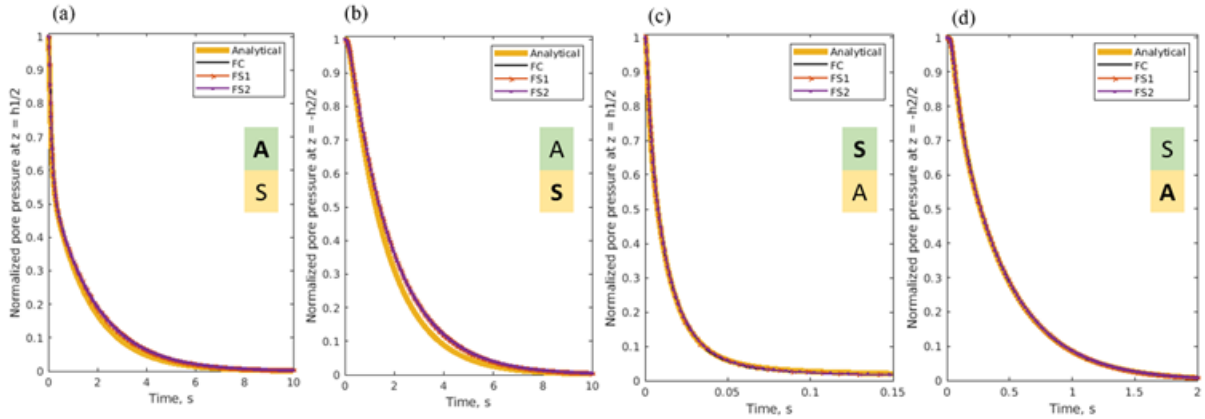

Figure 2-1. Pore pressure profile for two-layer Terzaghi problem at mid-point of each layer for (a-b) saline aquifer (A) top layer and sandstone (S) base layer and (c-d) sandstone (S) top layer and saline aquifer (A) base layer. Permeability (m^2) and elastic modulus (GPa) for saline aquifer and sandstone are 3×10^{-14} m^2 and 20 GPa, and 3×10^{-12} and 16 GPa, respectively. FC, FS1, and FS2 represent the fully coupled, fixed stress scheme implemented in Sierra/Aria, and fixed stress scheme implemented in Sierra/ Aria and Sierra/SM, respectively. Detailed description of models and other model results are available in Warren et al. (2022).

2.4. Evaluation of numerical coupling approaches for elasto-plasticity benchmark and experimental problems

This work (Yoon et al., in prep) is to evaluate the accuracy of Sierra/Aria and Sierra/SM on elasto-plasticity. After the yield point to which elasticity governs, the plastic behavior is nonlinear. In this work, two commonly used yield criteria models including Tresca (Tresca, 1869) and Drucker-Prager (Drucker and Prager, 1952) are evaluated. For 1D Terzaghi problem, we used a new analytical solution developed by Liu and Huang (2021) where plasticity starts at the drainage boundary and proceeds towards the undrained end. Since Sierra/Aria does not have a plastic material model, we evaluate the coupling solution using Sierra/Arpeggio where Sierra/Aria is used to solve for pore pressure and Sierra/SM is used to solve for displacement as described earlier. For plasticity, Drucker-Prager model is used. For 2D plate problem, the Galin plate with a hole at the center is used to analyze elasto-plastic behavior (Yarushina et al., 2010). Since the pore pressure is passive, only Sierra/SM is used to solve for mechanics. Plasticity starts at the edges of the central hole and extends into the plate. In the report, we briefly show one Terzaghi example in Figure 2-2. Comparison of numerical results with analytical solution shows that pore pressure, displacement, and the elasto-plastic interface location are well predicted. Although not reported here, the 2D plate problem also demonstrates a good accuracy of numerical solutions. As a part of validation, we also formulate the 2D elasto-plastic problem with the wellbore breakout test (Choens et al., 2019) where the pore pressure is passive and the wellbore in Mancos shale has a breakout, showing the progress of material failure. The progress of failure surface is treated as the advance of plasticity for model comparison.

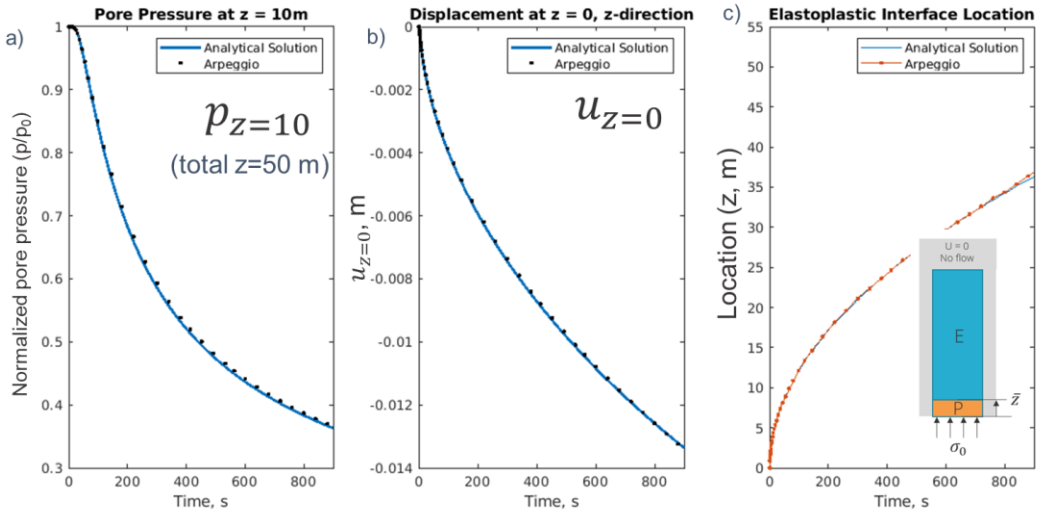

Figure 2-2. Comparison of numerical results (Sierra/Arpeggio) with the Analytical solution (Liu and Huang, 2021). a) Time history of the pore pressure at 10m from the drainage boundary, b) Time history of displacement at the drainage boundary (z = 0), and c) Time history of the location of the elasto-plastic interface, showing its progression along the height of the column over time. A schematic of 1D Terzaghi problem is shown in (c).

2.5. Thermo-poroelasticity

This section briefly describes the implementation and testing of thermo-poroelasticity for coupled energy transfer, fluid flow and deformation in an elastic porous material. Thermo-poroelasticity can be important for various subsurface energy and storage activities (enhanced geothermal recover, geologic carbon storage), heat driven methods (e.g., stream injection) for petroleum recovery and site remediation, geological nuclear waste disposal, among others. The constitutive model of linear thermo-poroelasticity, coupling thermal and mechanics to the flow equation follows the formulation described in the literature (e.g., McTigue 1986; Garipov et al., 2018). Energy conservation is modeled with an enthalpy-based energy balance. In this work we also implemented the fixed stress scheme for thermo-poroelasticity (Garipov et al., 2018) following the same procedure as for poroelastic problem described in the Section 2.2. Figure 2-3a shows a schematic of a 7m long column initially saturated with fluid at 1 Pa pressure, and subject to an external loading of 1 Pa. Like the Terzaghi consolidation problem, the upper boundary is drained, but in this version, the upper boundary temperature jumps to 50 °C, from 0 °C initially. Figure 2-3b shows the comparison of the consolidation of the upper boundary as a function of time from several researchers with our simulation results. Sierra/Aria results compared very well with that of Cui et al. (2018), and reasonably well with Garipov et al. (2018). Also, the fixed stress iteration (Aria_FS) and fully coupled (Aria_FC) schemes produced the same solution. In addition, the isothermal Terzaghi solution shows that in the heated condition, the consolidation initially follows the Terzaghi problem as the load transfers from the fluid to the solid with drainage at the upper boundary. However, later in time the heat is conducted into the column which begins to expand until reaching an asymptote as the whole column approaches the boundary temperature. This comparison shows that our implementation of fixed stress scheme into the Sierra software is completed properly.

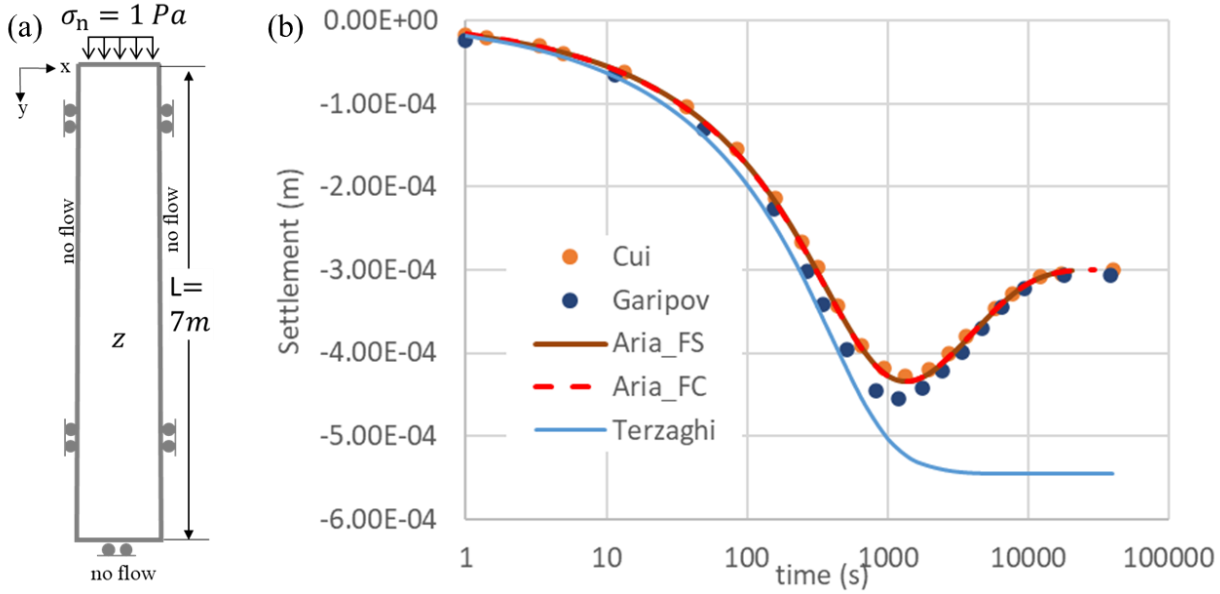

Figure 2-3. (a) A schematic of heated Terzaghi problem (redrawn from Cui et al., 2018) and (b) comparison of Sierra/Aria results with fixed stress (FS) and fully coupled (FC) schemes with the solutions from the literature and analytical solution of isothermal Terzaghi problem. Data in the literature are graphically obtained for this plot.

3. EFFECT OF CONFINED PRESSURE ON PERMEABILITY IN FRACTURED POROUS MEDIA

Flow and transport in fractured porous media play an important role in understanding many subsurface activities such as geologic carbon storage, enhanced geothermal energy, nuclear waste disposal, and nonproliferation. Furthermore, fracture geometry is deformed under confined stress conditions. Although quantification of fracture permeability under stress conditions has been investigated over the past decades, accounting for complexity of geomaterials in estimating fracture permeability to the subsurface is still a challenging task. As a part of validation of Sierra/Aria, in this work we identified the experimental data of stress-dependent permeability with key representative samples in which sample variability can cover a range of flow characteristics in fractured porous media. Detailed sample analysis with multiple imaging and analytical analysis has been conducted to examine the permeability changes under different confinements (i.e., stress). Finally, Sierra/Aria has been used to evaluate the experimental data to analyze how fracture and matrix permeabilities may respond to applied confined stress. This work is currently in preparation to submit for publication (Kucala et al., in prep).

3.1. Experimental samples

Three distinct fractured porous media have been identified and an example slice of 3D rock images obtained from micro-computed tomography (microCT) are presented in Figure 3-1. A size of samples are approximately 6.5 cm diameter and 6 cm height of cylindrical geometry. As shown, characteristics of flow in fractured porous media are different from fracture dominant to matrix-fracture dominant, depending on the fracture aperture sizes and connectivity and matrix pore connectivity. Permeability experiments with varying confined stresses have been performed in other projects (e.g., see Broome et al. (2018) for experimental testing description). For examples, permeability values of rhyolitic lava, vitric nonwelded, and zeolitic nonwelded samples shown in Figure 3-1 decreased from ~750, ~50, and ~500 milliDarcy (mD) under close to ambient conditions to 150, 17, and 100 mD under the maximum confinement of ~18 MPa, respectively.

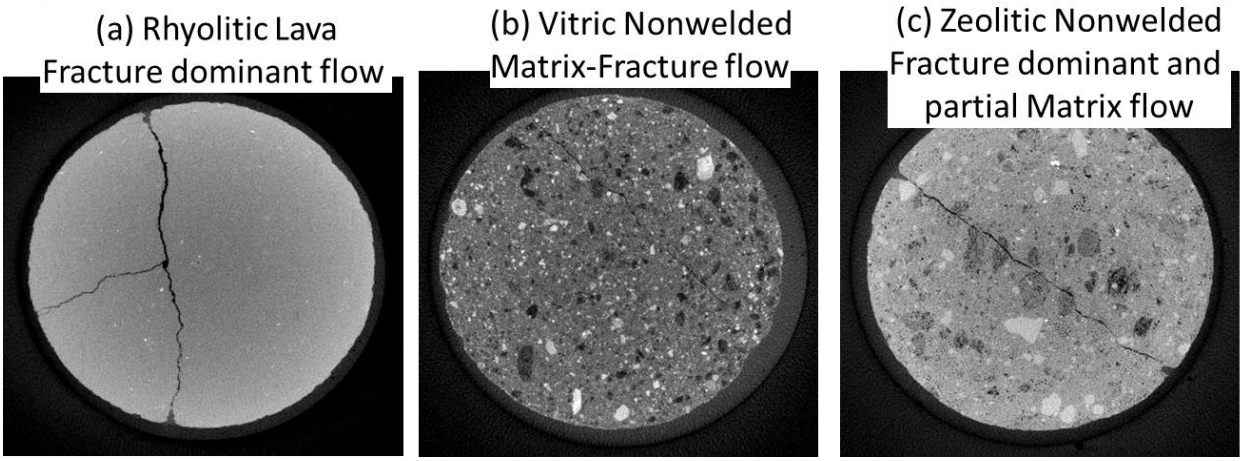

Figure 3-1. A slice of 3D microCT images of three experimental samples. (a) Rhyolitic Lava (RL) sample with fracture dominant flow, (b) Vitric Nonwelded sample (VN) with matrix-fracture flow, and (c) Zeolitic Nonwelded sample with fracture flow and partial matrix flow.

Figure 3-2 shows an example of initial fracture geometry. MicroCT images have been acquired after permeability testing is completed. Hence, non-elastic deformation in fracture geometry can't be accounted. In addition, the fracture roughness is not explicitly considered, hence we can use a relatively simple cubic law to represent the fracture permeability and aperture sizes and flow is at a laminar flow regime. The dependence of permeability (k) on the stress is represented by a commonly used exponential expression (Walsh, 1981), $k = k_0 \times \exp(-\alpha*(\sigma_0-\eta*p))$ where k_0 is the initial permeability (e.g., ambient pressure), α is the permeability stress sensitivity coefficient (1/MPa), σ_0 is the confinement pressure (MPa) in this study, η is the effective stress coefficient, and p is the pore pressure (Cao et al., 2019). For matrix deformation we use the same formula of stress-dependent permeability equation. However, α and η values are separately evaluated for fracture and matrix systems. With the cubic law and stress-dependent permeability equation, we compare numerical simulations with experimental results as shown in Figure 3-3.

To simplify the model system, we assume that fracture is vertically oriented. We first parameterize α and η values using analytical solution of fracture flow (e.g., Cao et al., 2019) where the fracture flow is estimated with the cubic law and stress dependent permeability equation. The difference between total measured flowrate and flowrate through fracture only is considered the flow fraction through matrix (i.e., non-fracture region). Once we finalize all parameters, we perform numerical simulations using Sierra/Aria with different meshes to evaluate the accuracy of model prediction against experimental data. As seen in Figure 3-3., simulation results with both volume mesh and shell element for fracture representation match experimental results well and a fraction of flow through matrix can be also estimated as in no fracture case. More detailed analysis will be reported in Kucala et al. (2022).

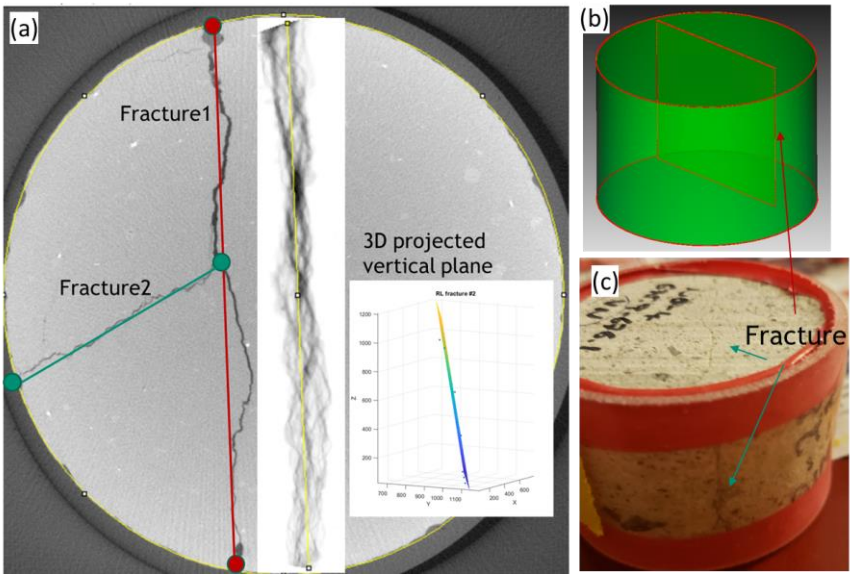

Figure 3-2. (a) An example of Rhyolitic Lava microCT image. One primary fracture (fracture 1) with a vertical orientation is expanded over the entire sample depth, while the secondary primary fracture (fracture 2) is through a half of the sample depth. An insert shows the projected fracture 1 over the entire depth and one projected plane from these 3D microCT images of fractures. (b) A numerical setup with a vertically oriented fracture. (c) A photo of RL sample. The fracture 1 is visually shown on top and side of the sample.

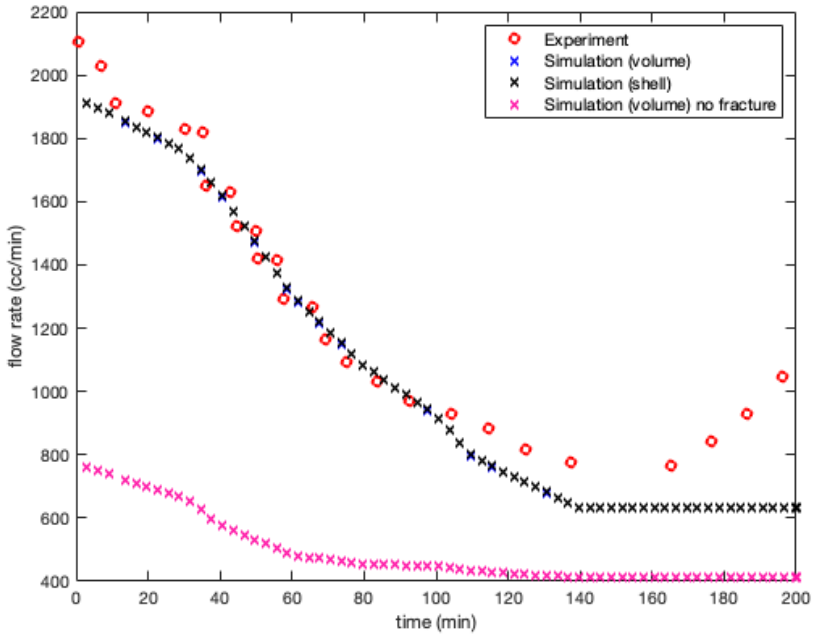

Figure 3-3. Comparison of numerical simulation results with experimental data of the Vitric Nonwelded sample (VN). Experimental data are averaged over a period of quasi steady state conditions of flowrates (~3-10 min). Three different simulations are performed with volumetric mesh in fracture and matrix (no fracture), and shell element representing fracture.

This page left blank

4. COUPLED POROELASTIC ANALYSIS OF FLUID INJECTION-INDUCED SEISMICITY

4.1. Hydromechanical controls on the spatiotemporal patterns of injection-induced seismicity in different fault architecture

This work is published in Chang and Yoon (2020) where the spatial and temporal patterns of injection-induced seismic events is studied to provide insightful information regarding the interaction between fluid injection activities and subsurface structures. This spatio-temporal relation can be used to infer the presence of undetected faults and/or fracture network associated with hydro-mechanical mechanisms. This study investigates the coupled flow and geomechanical control on the patterns of induced seismicity along multiple basement faults that show unusual spatio-temporal relation with induced seismicity far field first, followed by the near field. Two possible geological scenarios considered are (1) the presence of conductive hydraulic pathway within the basement connected to the distant fault and (2) no hydraulic pathway, but the co-existence of faults with mixed polarity as observed at Azle, TX. Based on the Coulomb stability analysis shown in Figure 4-1, simulation results show that direct pore-pressure diffusion through the hydraulic pathway to the distant fault can generate a larger number of seismicity than along the fault close to the injection well. Prior to pore-pressure diffusion, elastic stress transfer can initiate seismic activity along the favorably oriented fault, even at the longer distance to the well, which may explain the deep 2013–2014 Azle earthquake sequences. This study emphasizes that hydrological and geomechanical features of basement faults will locally control poroelastic coupling mechanisms, potentially influencing the spatio-temporal pattern of injection-induced seismicity, which can be used to infer subsurface architecture of fault/fracture networks.

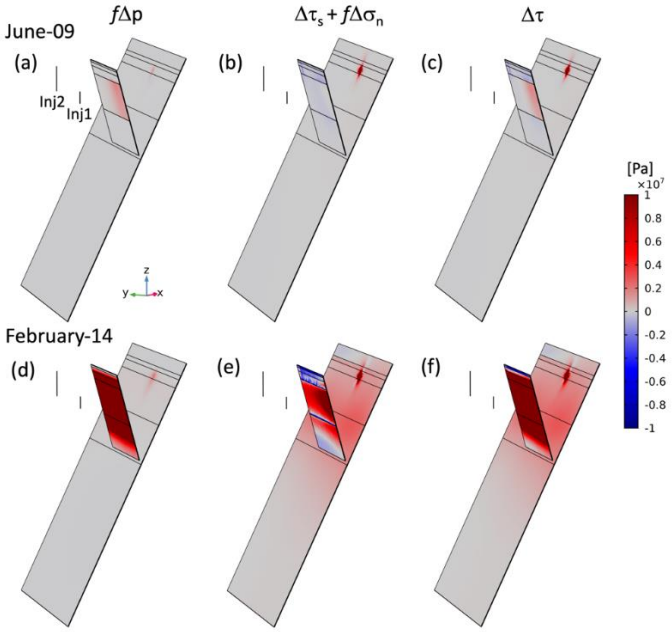

Figure 4-1. Spatio-temporal changes in Coulomb stress (Δτ) along the faults caused by fluid injection at Azle, TX in June of 2009 and February of 2014. Detailed analysis is reported in Chang and Yoon (2020). Inj1 and Inj2 show the locations of two injection wells, f is the frictional coefficient, Δp, $\Delta\tau_s$ and $\Delta\sigma_n$ represent the change in pore pressure, shear stress and normal stress, respectively. The colorbar shows the scale of the change in Pa.

4.2. Mitigating injection-induced seismicity along basement faults by extraction: Application to 2016–2018 Pohang earthquakes

This work is published in Chang and Yoon (2021) where the risk of induced earthquake is considered the major obstacle for sustainable subsurface energy activities. As a mitigation approach, mechanistic risk assessment can be essential to minimize the potential of seismic hazard. Coupled hydro-mechanical modeling approach is integrated with geomechanical analysis to better assess the occurrence of seismicity induced by injection and/or extraction, which will provide a basis to update operational conditions (e.g., number and location of mitigating wells, rate and duration of operations) for mitigating earthquake nucleation. The Coulomb stability analysis and seismicity rate estimation indicate that simultaneous extraction can relieve injection-induced pore-pressure buildup, but also transfer and accumulate elastic energy along the faults. Field-scale simulations with variation in well design for the Pohang enhanced geothermal system site, South Korea, show that multiple wells aligned across a preexisting fault form gradients of pressure and stress fields normal to the fault, which can enhance the direct impact of diffusion process and poroelastic stressing on the fault stability perturbation. Our mechanistic study suggests multiphysics-oriented mitigation strategies that consider (1) possible mechanical deformation, caused by hydro-mechanical coupling effects and (2) proper configuration of well operations based on site-specific geological characteristics.

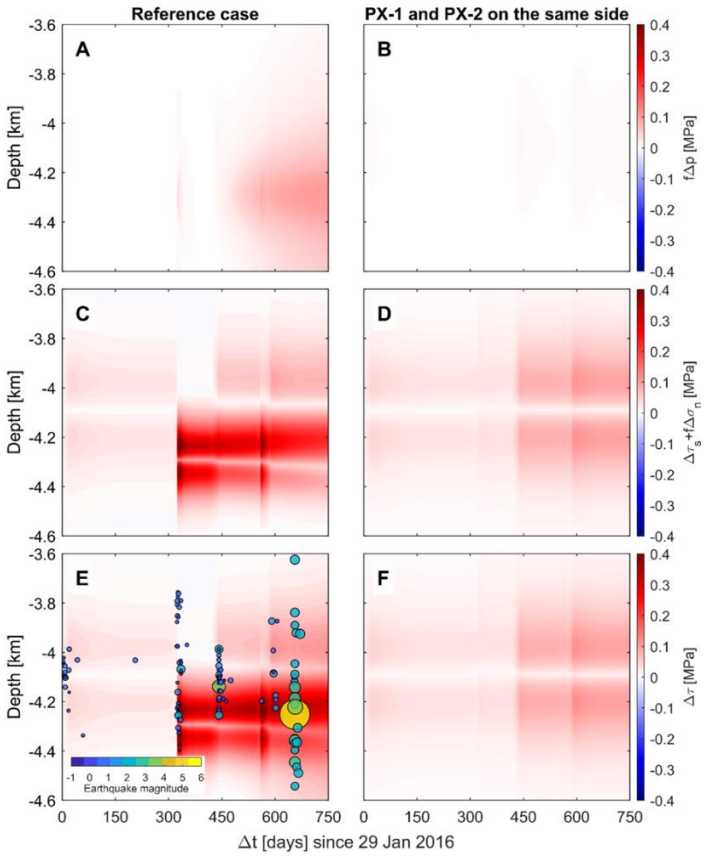

Figure 4-2. Temporal changes of Coulomb stress components along the fault at Pohang, South Korea with variation in the well location with respect to the fault location. The left column (A,C,E) shows the results from the reference case where two wells are located at each side of the fault, while the right column (B,D,F) shows the results from a comparative case where two wells are located at the same side of the fault.

4.3. Permeability-controlled migration of induced seismicity to deeper depths near Venus in North Texas

This work is published in Chang and Yoon (2022) where injection-driven interaction between pore-pressure diffusion and poroelastic stressing along preexisting basement faults and its relative significance in inducing seismicity are correlated spatially and temporarily to the propagation or retardation of pressure fronts corresponding to given operation history. Intense pore-pressure accumulation within a diffusion-dominant fault zone can nucleate moderate-to-large magnitude earthquakes even after shut-in. Steady transfer of elastic energy to the fault beyond the pressure fronts will increase stressing rate that may induce more frequent earthquakes of small magnitudes at large distance scales. This field-scale study shows that migrating patterns of 2015--2018 seismicity observed near Venus, TX (e.g., Chang and Yoon, 2020) are likely attributed to spatio-temporal evolution of both poroelastic mechanisms constrained by injection operations through multiple wells as well as hydraulic features of the fault.

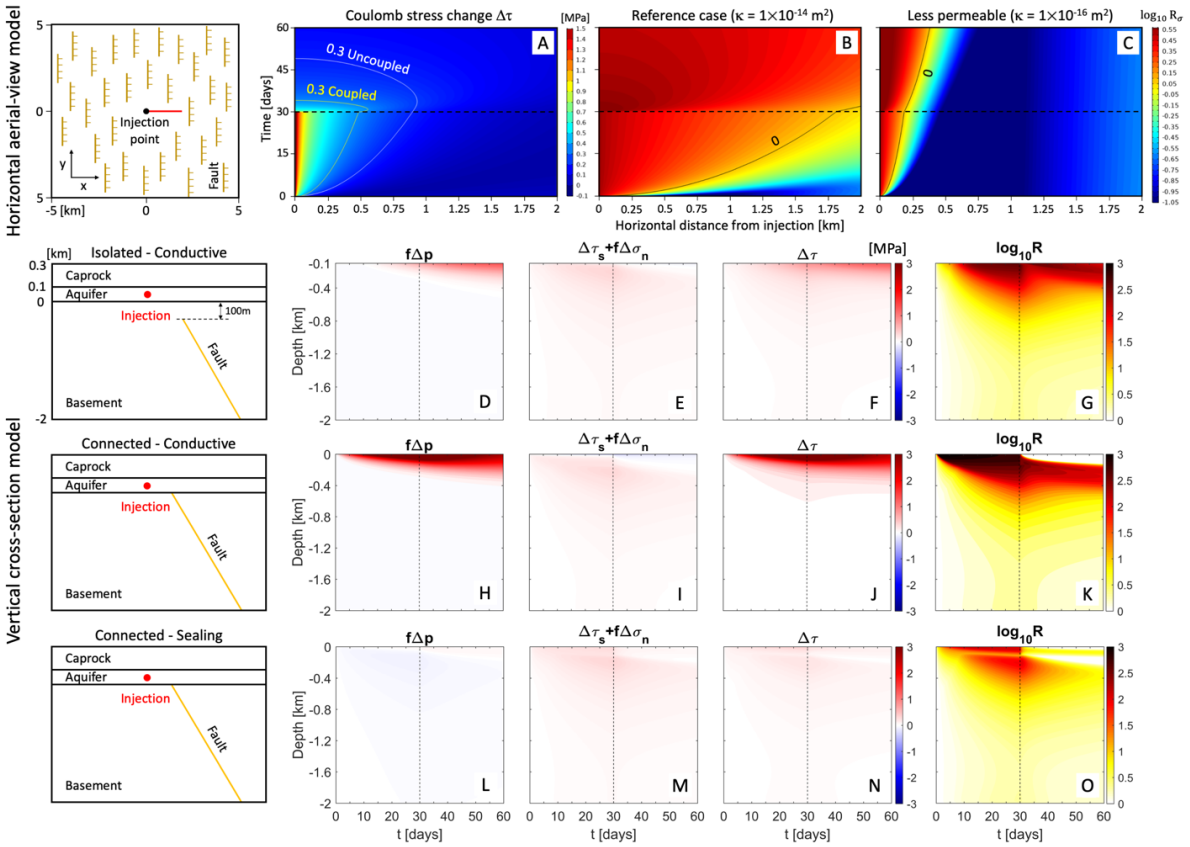

Figure 4-3. A) Coulomb stress change along the horizontal line in a 2-D aerial-view domain (a red line shown in the domain scheme) over time. To compute shear and normal tractions, faults (N-S striking and dipping 60° to east) are assumed to be uniformly distributed throughout the domain; hydrological and mechanical properties of the faults are the same as the background medium. (B--C) Spatio-temporal distribution of $\log_{10}R_\sigma$ (seismicity rate) for two formation permeability cases: (B) κ=1x10^{-14} m^2 and (C) κ=1x10^{-16} m^2 of less permeable formation. The contour of $\log_{10}R_\sigma$ =0 represents $f\Delta p = \Delta\tau_s + f\Delta\sigma_n$, such that diffusion and poroelastic stressing contribute equally to total changes in Coulomb stress. Spatio-temporal distribution of Coulomb stress components (D--F, H--J, L--N) and seismicity rate in a base 10 logarithmic scale (G, K, O) along the fault in a 2-D vertical domain for three fault types: (D--G) conductive, but hydraulically isolated from the aquifer,

(H--K) conductive and hydraulically connected, and (L--O) sealing. Black dashed line represents shut-in of injection, and the same color schemes are applied to the results of three fault cases. Detailed results are reported in Chang and Yoon (2022).

4.4. Potential Seismicity Along Basement Faults Induced by Geological Carbon Sequestration

This work is published in Chang et al. (2022) where large-scale CO_2 sequestration into geological formations is studied to evaluate a potential to induce earthquake along weak faults, which can be considered a negative impact on safety and public opinion. This study shows the physical mechanisms of potential seismic hazards along basement faults, either isolated from or connected to the injection layer, driven by CO_2 sequestration under variation in geological and operational constraints. We compare the poroelastic behaviors between multiphase flow and single-phase flow cases, highlighting specific needs of evaluating induced seismicity associated with CO_2 sequestration. In contrast to single-phase injection scenario, the contrast of fluid and rock properties between different structures will impact the pressure and stress fields, and slower migration of the CO_2 plume than pressure pulse may delay accumulation of pressure and stress along basement faults that may not be mitigated immediately by shut-in of injection. The impact of multiphase flow system, therefore, needs to be considered for proper monitoring and mitigation strategies, even though the gaseous plume does not penetrate into a low-permeability fault.

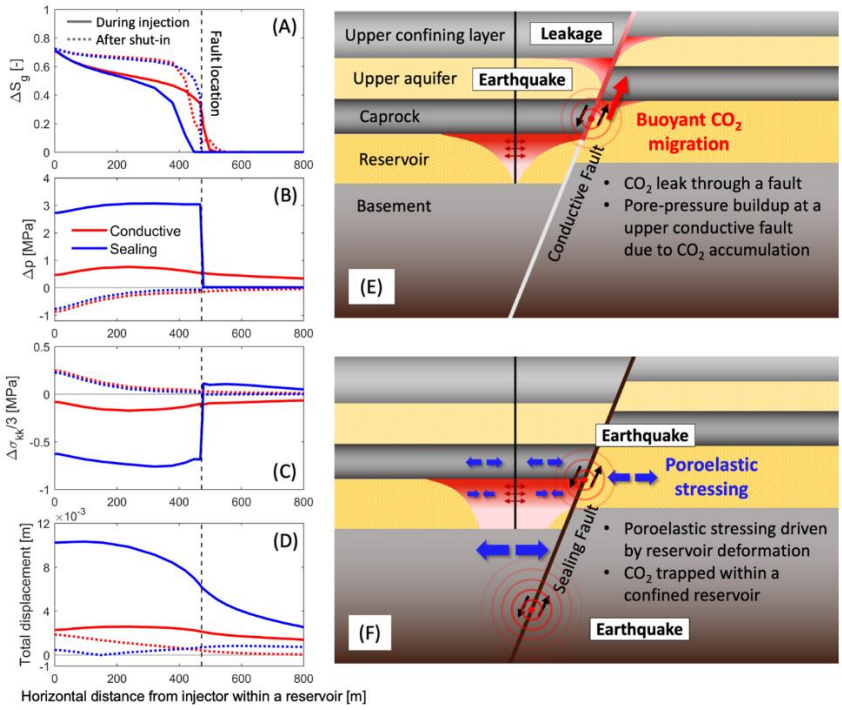

Figure 4-4. Modeling results with variation in fault permeability (red for conductive fault, κ_f=1x10^{-13} m^{2}and blue for sealing fault, κ_f=1x10^{-18} m^2, respectively) during injection (solid lines) and after shut-in (dash lines): (A to C) changes in CO_2 saturation, pore pressure, and mean stress along the middle of reservoir at 50 m below the caprock and (D) total displacement at the reservoir top. (E--F) Schematic description of dominant physical mechanisms of geohazards with the presence of either conductive or sealing fault, respectively.

5. MACHINE LEARNING DEVELOPMENT AND APPLICATIONS FOR FLOW, DEFORMATION, AND TEMPERATURE FIELD

5.1. Non-intrusive reduced order modeling of natural convection in porous media using convolutional autoencoders: comparison with linear subspace techniques

This work is published in Kadeethum et al. (2022a) where We adopt and present a non-intrusive reduced order model of natural convection in porous media, which is a highly nonlinear multiphysical problem relevant to many engineering applications (e.g., the process of CO_2 sequestration, magma flow, or bio-fluid mixing). Since high-fidelity models typically used to mimic these processes requires substantial computational resources because of their nonlinearity and the need for a very small time-step to satisfy Courant–Friedrichs–Lewy (CFL) condition resulting in not directly suitable to handle large-scale inverse problems, optimization, or control, in which an extensive set of simulations must be explored, we propose a non-intrusive reduced order model (ROM) of natural convection in porous media employing deep convolutional autoencoders for the compression and reconstruction and either radial basis function (RBF) interpolation or artificial neural networks (ANNs) for mapping parameters of partial differential equations (PDEs) on the corresponding nonlinear manifolds. The ROM is much faster than the high-fidelity model. Besides, our framework is not bound by the CFL condition; therefore, it could deliver quantities of interest at any given time, contrary to the high-fidelity model. Our model also offers a decent accuracy with a maximum relative error of 7%. We also provide comprehensive comparisons among approaches that rely on linear or nonlinear manifolds. We illustrate that in specific settings, the nonlinear compression outperforms its linear counterpart and vice versa. We suggest that it might be possible to use a quantitative comparison of subspace visualization using principal component analysis (PCA) and t-Distributed Stochastic Neighbor Embedding (t-SNE) to indicate which method will perform better.

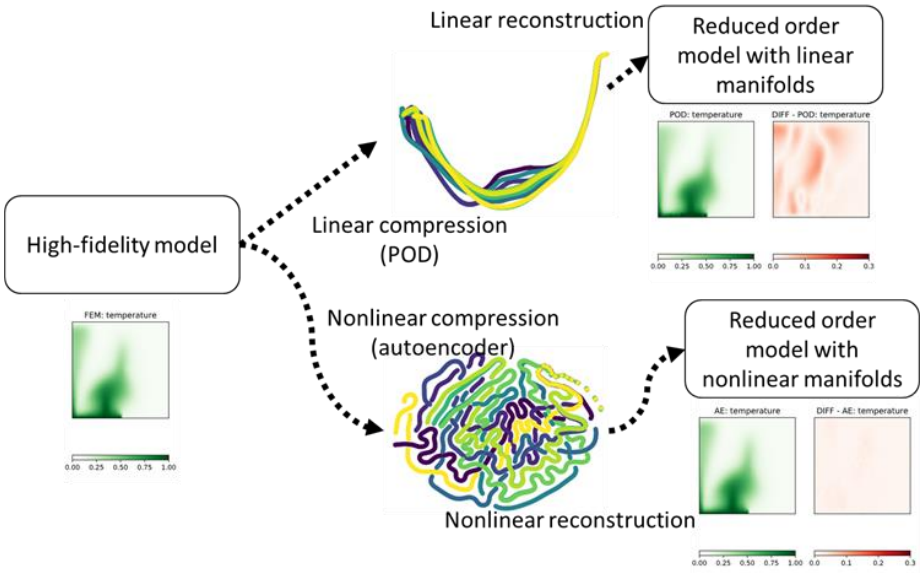

Figure 5-1. a framework proposed by this work. We compress a data produced by high-fidelity model through either linear or nonlinear compressions. ROM then reconstruct these manifolds through either linear or nonlinear reconstruction. DIFF represents point-wise absolute error.

5.2. Continuous conditional generative adversarial networks for data-driven solutions of poroelasticity with heterogeneous material properties

This work is published in Kadeethum et al. (2022b) where We present a non-intrusive reduced order modeling (ROM) for solving a time-dependent partial differential equations system. We showcase our framework's capability through coupled hydro-mechanical processes in heterogeneous porous media. These coupled processes commonly involve complex subsurface structures where the corresponding spatially distributed material properties can span several orders of magnitude and include discontinuous features (e.g., fractures, channels). Consequently, it is extremely difficult to parameterize heterogeneous spatial fields by a few parameters as traditional ROMs usually do. Our framework is developed upon continuous conditional generative adversarial networks (CcGAN) composed of the U-Net generator and patch-based critic. The generator has two variations: (1) the time domain is introduced to only the generator's bottleneck using element-wise addition and (2) the time domain is injected into all layers inside the generator through conditional batch normalization (. Our approach is desirable because it does not require any cumbersome modifications of full order model (FOM) source codes and can be applied to any existing FOM platforms. We illustrate that our framework could efficiently and accurately approximate finite element results given various permeability fields. Our results have a relative root mean square error of less than 2% with 10,000 samples for training. This robust framework will enable us to perform real-time reservoir management and robust uncertainty quantification in subsurface physics problems.

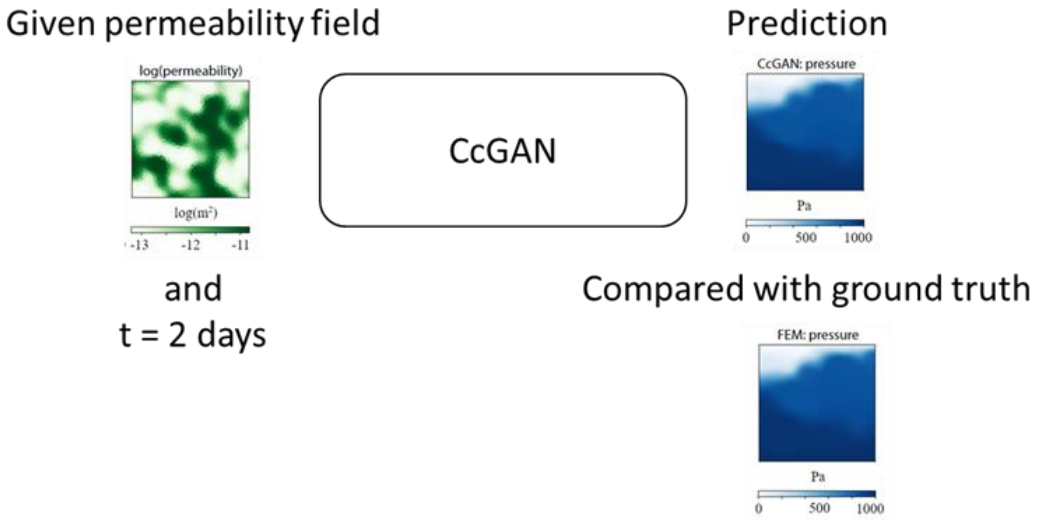

Figure 5-2. A framework proposed by this work. We use permeability field and time domain as an input. Subsequently, we predict quantities of interest (fluid pressure and bulk displacement in this case). Our prediction is very similar to that of the ground truth.

5.3. Reduced order modeling with Barlow Twins self-supervised learning: Navigating the space between linear and nonlinear solution manifolds

This work is published in Kadeethum et al. (2022c) where a reduced order model (ROM) is devised to provide an acceptable accuracy while utilizing a much lower computational cost than the full order model (FOM) or high-fidelity model. In recent years, a non-intrusive or data-driven ROM approach has grasped attention because (1) it has a straightforward implementation (i.e., it does not require any modifications of FOM), (2) it easily lends itself to different kinds of physical problems, and (3) it allows for a more stable and much faster prediction than intrusive ROM for nonlinear problems. Traditionally, proper orthogonal decomposition (POD) is used as a data compression tool (i.e., linear manifold approach), which is the optimal way to construct linear reduced manifolds. However, POD-based solutions on a linear subspace are often restrictive for highly nonlinear problems where reduced spaces lie in nonlinear manifolds. Deep learning ROM (DL-ROM) using deep-convolutional autoencoders (DC-AE) has been shown to capture nonlinear solution manifolds but fails to perform adequately when linear subspace approaches such as proper orthogonal decomposition (POD) would be optimal. Besides, most DL-ROM models rely on convolutional layers, which might limit their application to only a structured mesh. We propose a unified data-driven ROM that bridges the performance gap between linear and nonlinear manifold approaches. Moreover, this framework can handle unstructured meshes, which provides flexibility in its application to standard numerical solvers, on-site measurements, experimental data, or a combination of these sources. We show that the proposed framework achieves a relative error of 2% on average and 12% in the worst-case scenario (i.e., the training data is small, but the parameter space is ample.). We also show that our framework speeds up 7,000 times on average compared to FOM.

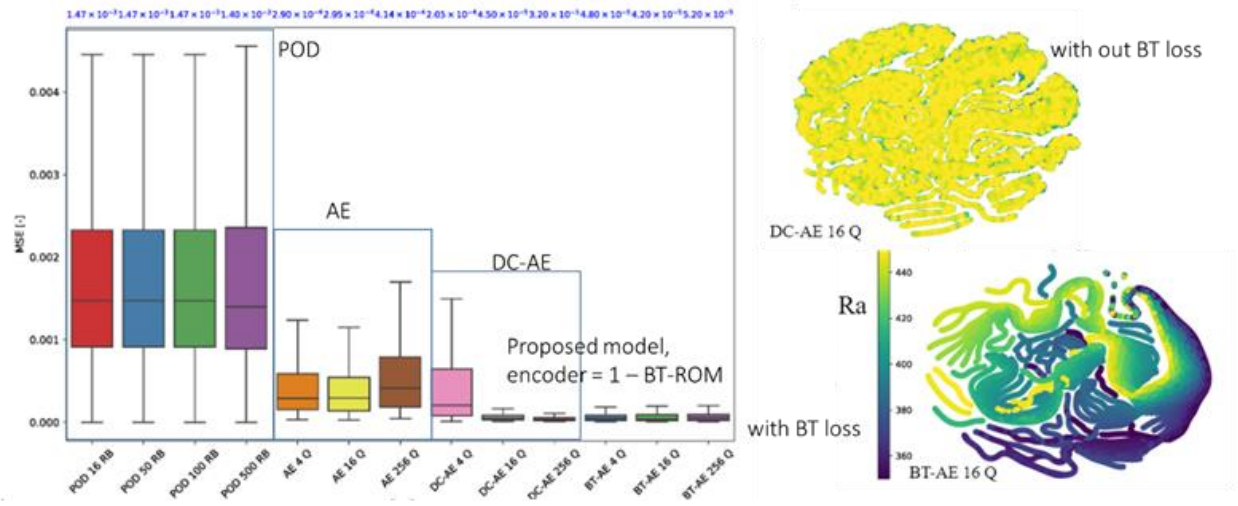

Figure 5-3. Barlow Twin (BT)-AE (proposed in this paper) performs better than the previous DL-ROM framework by providing comparable results to POD-based approaches for problems where the solution lies within a linear subspace as well as DL-ROM autoencoder-based techniques where the solution lies on a nonlinear manifold; consequently, bridges the gap between linear and nonlinear reduced manifolds. We illustrate that a proficient construction of the latent space is key to achieving these results, enabling us to map these latent spaces using regression models. We achieve the better structures reduced manifolds because Barlow Twins loss maximizes the information content of the embedding with the latent space through a joint embedding architecture.

5.4. Deep convolutional Ritz method: Parametric PDE surrogates without labeled data

This work is in review (Fuhg et al., in review) where convolutional neural networks (CNNs) are developed and applied for physical problems with a set of parameters represented by a weak form of partial differential equations (PDEs). CNNs are commonly trained to map input (sets of parameters) to output (PDE solutions) as data-driven ROM approaches. However, this approach relies on other models such as full order model (FOM) or other surrogate models to generate training data. To alleviate or remove the need of labelled data, convolutional physics-informed neural network (CPINN) to solve for the residual form of parametric PDEs have been proposed and applied for different physical problems (e.g., Gao et al., 2021, Ren et al., 2022). In this work (Fuhg et al., in review), an alternative formulation termed Deep Convolutional Ritz Method (DCRM) are proposed and evaluated as a parametric PDE solver. The term of Ritz method comes from the minimization of energy functionals, which has lower orders of the differential operators than residual-based methods using a strong form of PDEs. To evaluate the newly proposed DCRM, the Poisson equation with spatially parameterized source and boundary conditions is used to demonstrate that CNNs trained with relatively large training data (i.e., labelled data) perform better than CPINN in terms of training efficiency and generalization ability in terms of source and boundary conditions. However, DCRM approach without labelled data outperforms both CNNs and CPINN in terms of training efficiency and generalization ability, which may stem from the Ritz method, suggesting that DCRM has a potential to improve the training accuracy and efficiency without the need of training data.

5.5. Epistemic uncertainty-aware Barlow twins reduced order modeling

This work is in preparation for submitting to a Journal (Kadeethum et al., in prep) where Barlow twins reduced order modeling (BT-ROM) with uncertainty quantification (UQ-BT-ROM) has been proposed and evaluated for emulating high-fidelity models of nonlinear contact problems. Specifically, we extend the BT-ROM, which delivers better-reduced manifolds' structure obtained from a self-supervised learning framework to maximize the information content of the embedding with the latent space through a joint embedding architecture, to provide estimates of the epistemic uncertainty in our predictions caused by using a finite amount of training data. Adversarial training is used to train an ensemble of BT-ROM and identify lower-dimensional nonlinear manifolds endowed with Gaussian error estimates that quantify the epistemic reconstruction error. We showcase the UQ-BT-ROM framework through a series of problems involving contact between a rigid indenter and a hyperelastic substrate at finite deformations. The UQ-BT-ROM outperforms the BT-ROM as well as the intrusive ROM with Galerkin projection. The model's relative error is approximately 3% to 8% and can deliver a prediction with a fraction of the cost required by high-fidelity models (at least four orders of magnitude cheaper). We also illustrate that as we increase the amount of training data, our framework provides more accurate results and narrower prediction intervals. As a result, this framework can guild us in selecting optimal amounts of training data.

6. DYNAMIC SOIL PROPERTIES UDNER IMPACT TESTING AT AN INTERMEDIATE SCALE

This task is to develop a new experimental protocol and provide new experimental datasets to describe the behavior of geomaterials subjected to impact loading. Especially this research aims to develop new techniques for characterizing geomaterials subjected to impact and intermediate rate loads to produce robust datasets. These datasets can be crucial to calibrate and validate material models, such as those being developed in Sandia Sierra Mechanics software.

In this work, ultra-highspeed hydraulic actuators at the Blast, Shock and Impact Laboratory at Georgia Tech (Figure 6-1) are utilized to induce forces on intermediate-scale test articles for durations on the order of milliseconds with controlled acceleration and deceleration loading profiles. Because of the unique testing environment, the applied impulsive loads can be directly measured on both the impact and reaction side of the specimen and the material can be evaluated throughout the loading via cameras (i.e., digital image correlation) or other instrumentation. After impact, the specimens can also be quasi-statically loaded in-situ to quantify the residual capacity of the material, thus generating datasets that are not achievable with other methods. The research is divided into two main phases.

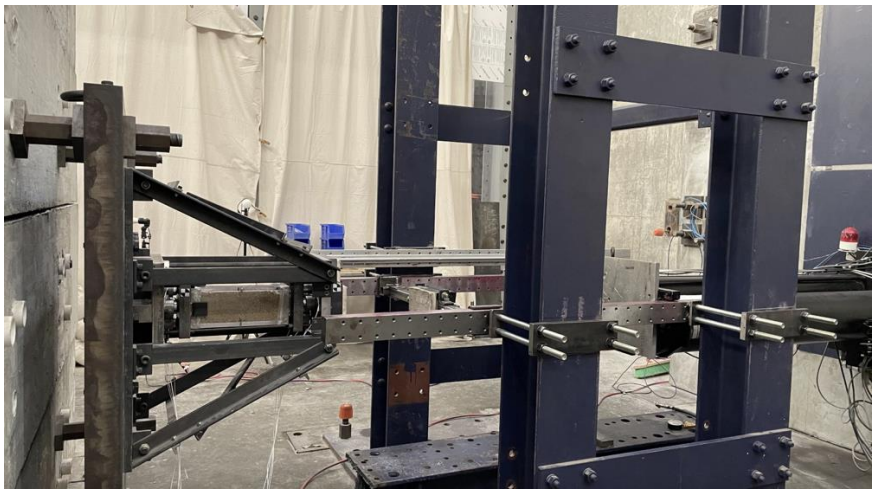

Figure 6-1. Hydraulic actuator at the Blast, Shock, and Impact Laboratory at Georgia Tech.

The first phase is to focus on development of new experimental technique for impulsively loaded compacted soils at an intermediate scale. To house the compacted soils, different materials (hard steel, transparent polycarbonate cylinder and square column, and flexible membrane) are evaluated to optimize the experimental apparatus and associated protocol for higher-rate loading regimes. An example of load cell design and prototype of polycarbonate cylinder is also shown in Figure 6-1(c-d). Key aspects of testing protocol to perform impact testing on compacted soils are the followings:

- Instrumentation: Dynamic load cells will measure impact force and reaction force
- Pressure and strain gauges can be installed to measure radial strain and high-speed cameras to measure cylinder axial displacement, achieving realtime measurements.

The second phase is to create datasets for modeling efforts with the most impactful parameters and uncertainties. Parametric studies using LS-DYNA simulations are conducted to create the multi-

variable datasets. It is expected that these datasets will contribute to the determination of key parameters of interest in the geomaterial models.

In summary, initial experimental modeling and design including preliminary numerical simulations and extensive literature review are completed. Initial experimental prototyping and fabrication in the laboratory are also completed. Based on the preliminary results, membrane was an optimal material to hold compacted soils and experimental iterations and protocol development with membrane sample holder are completed. The complete datasets generated in this section will be used to advance an intermediate scale impact testing of geomaterials, and improve our nation's ability to control and improve non-proliferation monitoring, and to develop next generation software for coupled multiphysics processes for Earth Science programs.

6.1. Experimental technique development

To examine the local behavior of the soils during the high-speed impact test, the research team studied, fabricated, and tested three distinct specimen prototypes. Polycarbonate prototypes (Figure 6-2) were constructed using clear polycarbonate materials. The use of polycarbonate was selected due to its material properties, specifically its transparency which allows for observation of the soils contained within it and its relatively high stiffness value, compared to other polymer, transparent materials. Modifications to the steel framing were made to fit the 6-inch polycarbonate specimen.

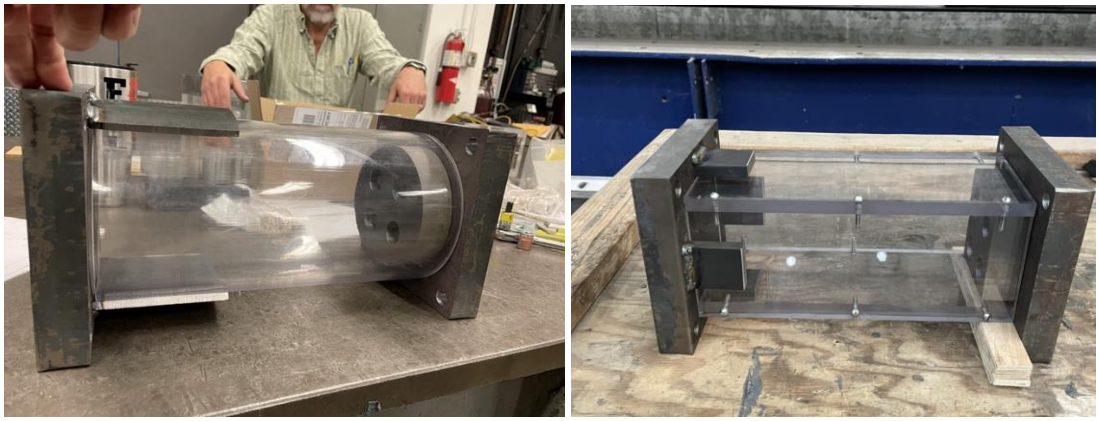

Figure 6-2. Experimental setup of polycarbonate prototype.

The second prototype (Figure 6-3) consisted of a flexible latex membrane such that the restraints imparted by the rigidity of the container were minimized, allowing for the observation of the strains and deformations of the soils through the deformation of the latex membrane. During the initial proof of concept experiments, dot patterns were traced in the membrane to evaluate the use of Digital Image Correlation (DIC) technology as a method to measure local deformations of the sample. The back and front supporting plates of the set up were modified to accommodate and support the geometry of the sample. Due to the lack of rigidity of the membrane, an additional support system was required to hold the sample in place during the testing. To do so, a lifting sling was used to support the front of the specimen during testing.

Figure 6-3. Experimental setup of latex prototype.

To measure the displacement and movement of the flyer plate as well as the front and back plates, high-speed cameras are used during the dynamic test. To measure force, eight Dytran 1061V6 piezometric force sensors are used. Four in the "impact" (front) plate and four in the "reaction" back plate. The four in the front plate measure the force of the flyer and the four in the back plate measure the reaction force on the other side of the sample. The progression of damage from the experiment from the latex prototype is given in Figure 6-4. The latex prototype was deemed the most successful as the polycarbonate fractured during impact. Therefore, this prototype will be refined and used to collect data to achieve the goals of the second phase.

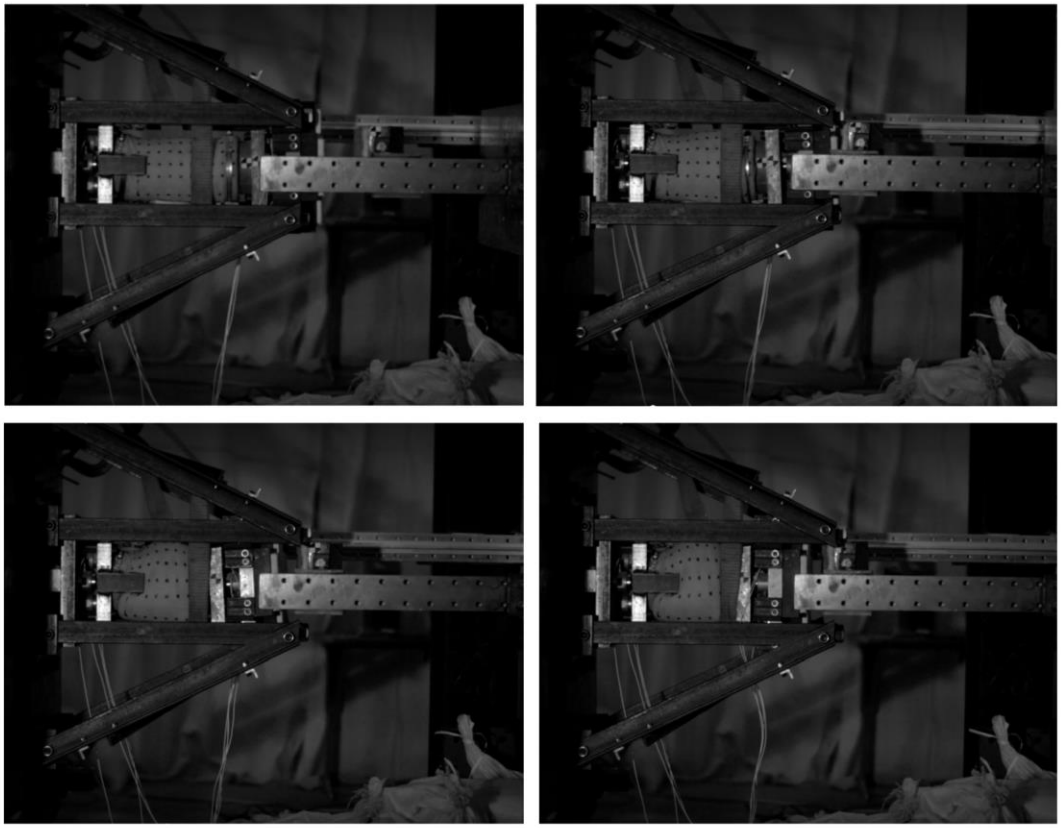

Figure 6-4. Examples of snapshots during experimental testing of impact on latex prototype.

REFERENCES

[1] Berre, I., Doster, F. and Keilegavlen, E., 2018. Flow in fractured porous media: A review of conceptual models and discretization approaches. Transport in Porous Media, pp.1-22

[2] Biot, M.A., 1941. General theory of three-dimensional consolidation. Journal of applied physics, 12(2), pp.155-164. http://dx.doi.org/10.1063/1.1712886.

[3] Broome, S.T., Ingraham, M. D., and Barrow, P. C., 2018. Permeability and Direct Shear Test Determinations of Barnwell Core in Support of UNESE. SAND2018-9134. Sandia National Laboratories, NM, USA. https://doi.org/10.2172/1734478. https://www.osti.gov/servlets/purl/1734478.

[4] Cao, N., Lei, G., Dong, P., Li, H., Wu, Z. and Li, Y., 2019. Stress-dependent permeability of fractures in tight reservoirs. Energies, 12(1), p.117.

[5] Chang, K. W., & Yoon, H., 2020, Hydromechanical Controls on the Spatiotemporal Patterns of Injection-Induced Seismicity in Different Fault Architecture: Implication for 2013–2014 Azle Earthquakes. Journal of Geophysical Research: Solid Earth, 125(9), e2020JB020402

[6] Chang, K. W., & Yoon, H., 2021, Mitigating injection-induced seismicity along basement faults by extraction: Application to 2016–2018 Pohang earthquakes. Journal of Geophysical Research: Solid Earth. https://doi.org/10.1029/2020JB021486

[7] Chang, K.W., Yoon, H., 2022. Permeability-controlled migration of induced seismicity to deeper depths near Venus in North Texas. Sci Rep 12, 1382. https://doi.org/10.1038/s41598-022-05242-7.

[8] Chang, K.W., Yoon, H., Martinez, M.J., 2022. Potential Seismicity Along Basement Faults Induced by Geological Carbon Sequestration [Geophysical Review Letters, e2022GL098721]

[9] Chang, K.W., Yoon, H., In preparation, Impact of layered architecture along the interface of reservoir and bedrock formation on Induced seismicity [Scientific Report, October 2022]

[10] Choens, R. C., Lee, M. Y., Ingraham, M. D., Dewers, T. A., & Herrick, C. G. (2019). Experimental studies of anisotropy on borehole breakouts in Mancos Shale. Journal of Geophysical Research: Solid Earth, 124, 4119– 4141. https://doi.org/10.1029/2018JB017090.

[11] Coussy, O., 2010. Mechanics and Physics of Porous Solids. John Wiley & Sons, Ltd.

[12] Cui, W., DM Potts, L Zdravkovic, KA Gawecka, DMG Taborda, 2018, An alternative coupled thermos-hydro-mechanical finite element formulation for fully saturated soils, Computers and Geotechnics, 94, 22-30.

[13] Drucker DC, Prager W. 1952 Soil mechanics and plastic analysis for limit design. Q. Appl.Math. 10, 157–165. (doi:10.1090/qam/48291)

[14] Faybishenko, B., Benson, S.M. and Gale, J.E. eds., 2015. Fluid dynamics in complex fractured-porous systems (Vol. 210). John Wiley & Sons.

[15] Fuhg, J.N., Karmarkar, A., Kadeethum, T., Yoon, H. and Bouklas, N., Deep Convolutional Ritz Method: Parametric PDE surrogates without labeled data. [the Journal of Data-Centric Engineering, in review].

[16] H. Gao, L. Sun, J.-X. Wang,2021, Phygeonet: physics-informed geometry-adaptive convolutional neural networks for solving parameterized steady-state pdes on irregular domain, Journal of Computational Physics 428, 110079.

[17] Garipov, TT, P Tomin, R Rin, DV Voskov, HA Tchelepi, 2018, Unified thermo-compositional-mechanical framework for reservoir simulation, Computational Geosciences, 22:1039-1057.

[18] T. Kadeethum, F. Ballarin, Y. Choi, D. O'Malley, H. Yoon, N. Bouklas. 2022a, Non-intrusive reduced order modeling of natural convection in porous media using convolutional autoencoders: comparison with linear subspace techniques [Adv. In Water Res., p.104098]

[19] T. Kadeethum, D. O'Malley, Y. Choi, H.S. Viswanathan, N. Bouklas, H. Yoon, 2022b. Continuous conditional generative adversarial networks for data-driven solutions of poroelasticity with heterogeneous material properties, Computers & Geosciences, Volume 167, 105212.

[20] Kadeethum et al., 2022c. Reduced order modeling with Barlow Twins self-supervised learning: Navigating the space between linear and nonlinear solution manifolds [Sci. Rep., In Press]

[21] Kadeethum et al., Epistemic uncertainty-aware Barlow twins reduced order modeling [2022 Conference on Neural Information Processing Systems, in review]

[22] Kim J, Tchelepi HA, Juanes R., 2011. Stability and convergence of sequential methods for coupled flow and geomechanics: Fixed-stress and fixed-strain splits. Comput Methods Appl Mech Engrg. 200 (13–16), 1591–1606. http://dx.doi.org/10.1016/j.cma.2010.12.022.

[23] Kucala et al. Permeability evolution as a function of stress for three distinct fractured porous media [Geophysical Review Letters, in prep]

[24] Liu, M., & Huang, H. (2021). Finite element modeling of spherical indentation in a poro-elasto-plastic medium via step displacement loading. International Journal for Numerical and Analytical Methods in Geomechanics, 45(10), 1347-1380.

[25] Maria Warren, James E. Bean, Mario J. Martinez, Alec Kucala, Hongkyu Yoon, 2022, Evaluation of accuracy and convergence of numerical coupling approaches for poroelasticity benchmark problems, Geomechanics for Energy and the Environment, Volume 31, 100352, https://doi.org/10.1016/j.gete.2022.100352.

[26] McTigue, DF, 1986, Thermoelastic response of fluid-saturated porous rock, J. of Geophysical Research, 91, No B9, 9533-9542.

[27] Merxhani, A., 2016. An introduction to linear poroelasticity. arXiv preprint arXiv:1607.04274.

[28] P. Ren, C. Rao, Y. Liu, J.-X. Wang, H. Sun, 2022, Phycrnet: Physics-informed convolutional-recurrent network for solving spatiotemporal pdes, Computer Methods in Applied Mechanics and Engineering 389, 114399.

[29] SIERRA/ARIA. 2021, SIERRA multimechanics module: Aria user manual - version 5.0. http://dx.doi.org/10.2172/1777075.

[30] SIERRA/Arpeggio. 2021. SIERRA code coupling module: Arpeggio user manual – version 5.0. http://dx.doi.org/10.2172/1777077.

[31] Sierra/SM, 2021. Sierra/SolidMechanics 5.0 user's guide. http://dx.doi.org/10.2172/1608404.

[32] Terzaghi K. Theoretical soil mechanics. 1943. http://dx.doi.org/10.1002/9780470172766.

[33] Terzaghi KV. Die berechnung der durchlassigkeitsziffer des tones aus dem verlauf der hydrodynamischen spannungserscheinungen. In: Sitzungsberichte Der Akademie Der Wissenschaften in Wien, Mathematisch-Naturwissenschaftliche Klasse, Vol. 132, Abteilung IIa, 1923. PP.125-138.

[34] Tresca H. 1869 Mémoire sur l'écoulement des corps solides. Paris, France: Imprimerie Impériale.

[35] Verruijt A., 2015. Theory and Problems of Poroelasticity. Delft University of Technology, Netherlands, https://geo.verruijt.net/software/PoroElasticity2015.pdf.

[36] Walsh, J.B. Effect of pore and confining pressure on fracture permeability. Int. J. Rock Mech. Min. 1981, 18, 429–435.

[37] Wang, H., 2000. Theory of linear poroelasticity with applications to geomechanics and hydrogeology (Vol. 2). Princeton university press.

[38] Yarushina, V.M., Dabrowski, M. and Podladchikov, Y.Y., 2010. An analytical benchmark with combined pressure and shear loading for elastoplastic numerical models. Geochemistry, Geophysics, Geosystems, 11(8). Q08006, doi:10.1029/2010GC003130.

[39] Yoon et al. Evaluation of accuracy and convergence of numerical coupling approaches for elasto-plasticity: benchmark problems and wellbore breakout experiment [In prep for submission to Computers & Geosciences]

DISTRIBUTION

Email—Internal

Name	Org.	Sandia Email Address
Tracy Woolever	8131	tawoole@sandia.gov
Benjamin K Cook	8900	bkcook@sandia.gov
Austin A Holland	8864	aaholla@sandia.gov
Hongkyu Yoon	8864	hyoon@sandia.gov
Technical Library	1911	sanddocs@sandia.gov

This page left blank

This page left blank

Sandia National Laboratories

Sandia National Laboratories is a multimission laboratory managed and operated by National Technology & Engineering Solutions of Sandia LLC, a wholly owned subsidiary of Honeywell International Inc. for the U.S. Department of Energy's National Nuclear Security Administration under contract DE-NA0003525.